

Gravitational drag on a point mass in hypersonic motion through a gaseous medium

J. Cantó¹, A. C. Raga^{2*}, A. Esquivel², F. J. Sánchez-Salcedo¹

¹*Instituto de Astronomía, Universidad Nacional Autónoma de México, Ap. 70-468, 04510 D. F., México*

²*Instituto de Ciencias Nucleares, Universidad Nacional Autónoma de México, Ap. 70-543, 04510 D. F., México*

ABSTRACT

We explore a ballistic orbit model to infer the gravitational drag force on an accreting point mass M , such as a black hole, moving at a hypersonic velocity v_0 through a gaseous environment of density ρ_0 . The streamlines blend in the flow past the body and transfer momentum to it. The total drag force acting on the body, including the nonlinear contribution of those streamlines with small impact parameter that bend significantly and pass through a shock, can be calculated by imposing conservation of momentum. In this fully analytic approach, the ambiguity in the definition of the lower cut-off distance r_{\min} in calculations of the effect of dynamical friction is removed. It turns out that $r_{\min} = \sqrt{e}GM/2v_0^2$. Using spherical surfaces of control of different sizes, we carry out a successful comparison between the predicted drag force and the one obtained from a high resolution, axisymmetric, isothermal flow simulation. We demonstrate that ballistic models are reasonably successful in accounting for both the accretion rate and the gravitational drag.

Key words: black hole physics – hydrodynamics – ISM: kinematics and dynamics – ISM: clouds – stars: formation

1 INTRODUCTION

A body moving in a background medium loses momentum due to its gravitational interaction with its own gravitationally induced wake. This process is often referred to as dynamical friction. Chandrasekhar (1943) estimated the dynamical friction on a massive particle passing through a homogeneous and isotropic background of light stars. In the case where the perturber moves in a gaseous medium, the gravitational drag is traditionally inferred as the gravitational attraction between the perturber and its own wake. In this approach, the density structure of the wake is derived in linear perturbation theory by assuming that the body produces a small perturbation in the ambient medium (Dokuchaev 1964; Ruderman & Spiegel 1971; Just & Kegel 1990; Ostriker 1999; Kim & Kim 2007; Sánchez-Salcedo 2009; Namouni 2010). For a perturber moving on a rectilinear orbit at constant velocity, the steady-state linear theory predicts that the drag force vanishes for subsonic perturbers, while it becomes similar to the collisionless drag force for supersonic bodies. Ostriker (1999) considered the linear-theory drag as a time-dependent rather than steady state problem and arrived at the following formula for the gravitational drag force,

$$F_g = \frac{4\pi\rho_0 G^2 M^2}{v_0^2} \begin{cases} \frac{1}{2} \ln\left(\frac{1+\mathcal{M}}{1-\mathcal{M}}\right) - \mathcal{M} & \text{if } \mathcal{M} < 1; \\ \frac{1}{2} \ln(1 - \mathcal{M}^{-2}) + \ln\left(\frac{v_0 t}{r_{\min}}\right) & \text{if } \mathcal{M} > 1. \end{cases} \quad (1)$$

The perturber of mass M , which moves at velocity v_0 and Mach number \mathcal{M} in a rectilinear orbit through a homogeneous medium with density ρ_0 and sound speed c_0 , is assumed to be formed at $t = 0$. The minimum radius r_{\min} is the typical size of the perturber. This formula has enjoyed widespread theoretical application (Narayan 2000; Escala et al. 2004; Kim 2007; Conroy & Ostriker 2008; Villaver & Livio 2009; Tanaka & Haiman 2009; Nejad-Asghar 2010; Chavarria et al. 2010). Because of the linear-theory assumption, the above equation is properly valid only at $r \gg R_{\text{BH}}$ where R_{BH} is the Bondi-Hoyle radius ($R_{\text{BH}} \equiv GM/[c_0^2(1 + \mathcal{M}^2)]$). Therefore, Equation (1) is strictly valid for extended perturbers with a softening radius much larger than the Bondi-Hoyle radius. In fact, for extended perturbers, Sánchez-Salcedo & Brandenburg (1999) found good agreement between the gravitational drag in full hydrodynamical simulations and Ostriker’s formula. In particular, for Plummer perturbers with softening radius r_s much larger than R_{BH} , they found that $r_{\min} = 2.25r_s$. An extension of Ostriker’s formula for extended bodies orbiting in a stratified gaseous sphere was given in Sánchez-Salcedo & Brandenburg (2001).

* E-mail: raga@nucleares.unam.mx

In the case of point-like perturbers, like massive black holes, it is reasonable to assume that r_{\min} should be of the order of a few R_{BH} , but a nonlinear analysis is required to fix the uncertainty in the definition of r_{\min} . In adiabatic simulations of axisymmetric accretion flows past a gravitating absorbing object, Shima et al. (1985) computed the drag by considering two contributions: the aerodynamic force, which is due to the accretion of momentum over the body surface, and the gravitational force on the perturber by its own wake. They found that the numerical results were consistent with the estimates in linear theory.

The problem of the gravitational drag on a point-mass particle has revived new interest to estimate the timescale of the orbital decay of massive black hole binary in the centre of galaxies. Escala et al. (2004) simulated the orbital decay of a single black hole moving initially on a circular orbit in an isothermal gaseous sphere. They found that the gravitational drag is less peaked at $1 \leq \mathcal{M} < 2$ than predicted by Ostriker's formula with $\ln v_0 t / r_{\min} = 3.1$. Tanaka & Haiman (2009) combined the prescriptions of Ostriker (1999) and Escala et al. (2004) into a formula that is used as a prescription of the gaseous drag on black holes in numerical simulations. In order to isolate the physical reason of the failure of Ostriker's formula, Kim & Kim (2009) and Kim (2010) carried out axisymmetrical simulations of a massive body in rectilinear orbit with different values of the strength of the gravitational perturbation due to the body as measured by

$$\mathcal{A} = \frac{GM}{c_0^2 r_s}, \quad (2)$$

where r_s is the softening radius of the Plummer perturber. They find that the functional form of the gravitational drag is not so peaked as the linear theory predicts and conclude that the discrepancy between the numerical and Ostriker results are most likely due to the nonlinear effect. It is important to note that in the simulations of Escala et al. (2004), Kim & Kim (2009) and Kim (2010), the perturber simply provides a smooth gravitational potential and does not hold any absorbing surface. Without any absorbing inner boundary condition, a hydrostatic envelope with front-back symmetry is formed near the perturber. Because of the front-back symmetry, this large envelope provides a negligible contribution to the gravitational drag force.

However, it is well-known that accretion is a crucial ingredient in point-like objects, such as black holes or stars. Different boundary conditions in the high density region of the wake are expected to change the gas dynamics near the perturber and the strength of the gravitational drag (e.g., Fryxell et al. 1987; Naiman et al. 2011). For example, Ruffert (1996) simulated a 3D quasi-isothermal flow with an absorbing boundary surrounding the point-like object. Moeckel & Throop (2009) carried out similar simulations, but then also included an accretion disk orbiting the point source.

The aim of this paper is to describe the contribution of the nonlinear inner wake to the gravitational drag on hypersonic perturbers by using the ballistic orbit theory (Bondi & Hoyle 1944; Lyttleton 1972; Bisnovatyi-Kogan et al. 1979). Whereas this theory (the so-called model of line-accretion) has been extensively used as a powerful framework to describe the gravitational interaction between a moving massive body and the surrounding gaseous medium in the context of supersonic Bondi-Hoyle-Lyttleton accretion

(e.g., Koide et al. 1991; Edgar 2004), it has been traditionally ignored as a tool to quantify the gravitational drag. In fact, all analytical studies about the gravitational drag in gaseous media have been based on the linear perturbation theory, following on the analysis of Dokuchaev (1964), Ruderman & Spiegel (1971) and Rephaeli & Salpeter (1980). In this paper we develop the ballistic orbit theory to provide analytical expressions of, not only the mass accretion rate, but also the nonlinear drag force on a hypersonic compact body. These estimates will be compared with numerical results of an axisymmetric isothermal hydrodynamical simulation.

2 THE FREE-STREAMING FLOW SOLUTION

Let us consider the axisymmetric flow generated by a point mass M which moves hypersonically at a constant velocity v_0 inside a homogeneous gaseous environment (see also Bisnovatyi-Kogan et al. 1979). Fig. 1 shows a schematic diagram illustrating the trajectory of a fluid parcel in a frame of reference at rest with respect to the point mass.

Because v_0 (the upstream environmental velocity, see Fig. 1) is hypersonic, we neglect the pressure force and consider the ballistic trajectory of the fluid parcels in the gravitational potential of the point mass. As they have a positive $E = v_0^2/2$ energy (per unit mass), the trajectories of the fluid parcels are hyperbolae of the form :

$$r = \frac{\xi^2}{\xi_0 (1 + \cos \theta) + \xi \sin \theta}, \quad (3)$$

where ξ is the impact parameter of the fluid parcel (see Fig. 1) and

$$\xi_0 \equiv \frac{GM}{v_0^2}, \quad (4)$$

with G being the gravitational constant. For deriving Eq. (3) one has to consider a generic hyperbolic trajectory of the form $r = p/[1 + \epsilon \cos(\theta - \theta_0)]$, and then impose the upstream boundary condition and the conserved angular momentum ξv_0 to determine the constants p , ϵ and θ_0 .

From Eq. (3), we see that the streamline intercepts the symmetry axis (i.e. $\theta = 0$, see Fig. 1) at a position

$$x_0 = \frac{\xi^2}{2\xi_0}, \quad (5)$$

downstream from the perturber. The material will therefore pile up in a narrow, downstream wake surrounding the symmetry axis, forming a dense column of gas.

From the equation for the streamlines (Eq. 3) one can calculate the velocity components of the free-streaming flow along the x and y -axes :

$$v_x = \frac{v_0}{\xi} (\xi + \xi_0 \sin \theta); \quad v_y = -\frac{v_0 \xi_0}{\xi} (1 + \cos \theta). \quad (6)$$

Assuming that the environment has a homogeneous density ρ_0 far upstream from the source, it is possible to obtain the density $\rho(x, y)$ of the free-streaming flow as a function of position:

$$\frac{\rho}{\rho_0} = \frac{\xi^3}{y[2\xi_0(r+x) + \xi y]} = \frac{\xi^2}{y(2\xi - y)}, \quad (7)$$

with

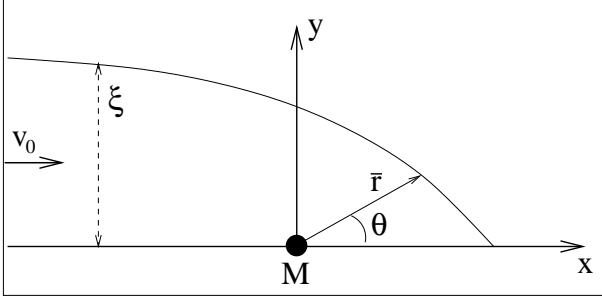


Figure 1. Schematic diagram showing the trajectory of an environmental fluid parcel in hypersonic motion with respect to a point mass M . The initial velocity v_0 of a parcel with impact parameter ξ is parallel to the x -axis, and its trajectory is the $\bar{r}(\theta)$ curve. The problem has cylindrical symmetry, with x being the symmetry axis and y the cylindrical radius.

$$r = \sqrt{x^2 + y^2}; \quad \xi = \frac{1}{2} \left[y + \sqrt{y^2 + 4\xi_0(r+x)} \right]. \quad (8)$$

Note that x is the distance along the symmetry axis and y the cylindrical radius. It is simple to see that $\rho \geq \rho_0$. Equation (7) is not valid in the shocked column of gas near the positive x -axis. The density enhancement in this approach is different from that derived in linear theory which predicts zero-enhancement outside the Mach cone (e.g., Ostriker 1999). Koide et al. (1991) found a good accordance between the analytical solutions (6)-(8) and the numerical solution even for Mach numbers as low as 1.4.

From Eq. (6) we see that at the point in which the streamlines intercept the symmetry axis (i.e., for $\theta = 0$), the flow velocity has an x -component $v_x(0) = v_0$ (identical to the far upstream flow velocity and independent of the impact parameter ξ of the flow parcel) and a y -component $v_y(0) = -2v_0\xi_0/\xi$. This latter component of the velocity will be thermalized in a shock surrounding the downstream wake. We will assume that the post-shock thermal energy is radiated away instantaneously.

Now, the kinetic+potential energy per unit mass of the flow at $x \rightarrow -\infty$ is $E_0 = v_0^2/2$. When the flow hits the symmetry axis (at $\theta = 0$), the energy associated with the y -velocity is thermalized, so that the kinetic+potential energy is reduced to a value

$$E_t = E_0 - \frac{v_y^2(0)}{2} = \frac{v_0^2}{2} \left[1 - \left(\frac{2\xi_0}{\xi} \right)^2 \right]. \quad (9)$$

From Eq. (9) it is clear that $E_t \leq 0$ (i.e., the post-shock material is gravitationally bound) if the condition

$$\xi \leq 2\xi_0 \quad (10)$$

is met. Therefore all of the material arriving with impact parameters $\leq 2\xi_0$ will eventually be accreted onto the body. A streamline with impact parameter $\xi_1 = 2\xi_0$ (with ξ_0 given by Eq. 4) crosses the symmetry axis at a distance

$$x_1 = 2\xi_0, \quad (11)$$

downstream from the body (see Eq. 5 and Fig. 1).

The material within the downstream wake will have a complex flow pattern. From Eq. (6) it is clear that the material enters the tail with a positive x -velocity. The material with impact parameter $\xi \leq 2\xi_0$ (which is gravitationally bound, see above) will therefore enter the wake flowing in

the $+x$ -direction, so that it will first flow away from the body, and eventually reverse and fall back onto the body. The distance x_m from the body (along the x -axis) at which the flow reverses can be obtained from the condition of zero velocity for a radial motion in the gravitational potential. This condition gives :

$$x_m = \frac{2\xi_0}{(2\xi_0/\xi)^2 - 1}. \quad (12)$$

We see that when $\xi \rightarrow \xi_1$, $x_m \rightarrow \infty$. Consequently, streamlines with impact parameter close to and smaller than ξ_1 , will take a long time to be accreted.

The material in the wake that remains gravitationally unbound when entering the wake (i.e., the material with impact parameters $\xi > 2\xi_0$, see above), will flow away from the body along the x -axis, reaching infinity with a velocity

$$v_\infty = v_0 \left[1 - \left(\frac{2\xi_0}{\xi} \right)^2 \right]^{1/2}. \quad (13)$$

3 THE MASS ACCRETION RATE AND THE DRAG FORCE

3.1 The accretion rate

From the solution of section 2, the accretion rate onto the point mass can be obtained (Hoyle & Lyttleton 1939; Bondi & Hoyle 1944). All of the material with impact parameters $\xi \leq 2\xi_0$ (see eq. 10) will fall onto the body. Therefore, the mass accretion rate is:

$$\dot{M}_{acc} = \pi(2\xi_0)^2 \rho_0 v_0 = \frac{4\pi(GM)^2 \rho_0}{v_0^3}, \quad (14)$$

where we have used Eq. (4) for the second equality.

3.2 The gravitational drag

We calculate the gravitational drag on the perturber by computing the net x -momentum per unit of time, $\dot{\Pi}_x$, going through a spherical control volume of radius $R > 2\xi_0$ centred on the body. It is clear that the contribution to the drag by the gas within the sphere is equal to $\dot{\Pi}_x$.

We consider the three streamlines shown in the schematic diagram of Fig. 2 :

- a streamline with impact parameter $\xi_1 = 2\xi_0$, which crosses the axis at $x_1 = 2\xi_0$ (see eq. 11). All of the material with $\xi \leq \xi_1$ is accreted onto the body,
- a streamline with impact parameter $\xi_2 = \sqrt{2\xi_0 R}$, which crosses the axis at a distance R downstream from the perturber (where R is the radius of the control sphere, see above),
- a streamline with impact parameter ξ_3 , which tangentially touches the control sphere (at a point with polar angle θ_3 , see Fig. 2).

In order to obtain ξ_3 and θ_3 we first set $r = R$ (i.e., a radius equal to the radius of the control sphere) in Eq. (3), and invert this equation to find :

$$\sin \theta_{\pm} = \frac{\xi \left[\xi^2 - \xi_0 R \pm \xi_0 \sqrt{R(2\xi_0 + R) - \xi^2} \right]}{R(\xi^2 + \xi_0^2)}, \quad (15)$$

which gives the two values of θ at which the streamline with impact parameter ξ cuts the control sphere. The angle θ_+ (obtained with the + sign of the right hand term of Eq. 15) corresponds to the point in which the streamline enters the control sphere, and θ_- corresponds to the exit point. For the tangential streamline (with impact parameter ξ_3 , see Fig. 2) the entry and exit points coincide, so that the term within the square root of Eq. (15) has to be equal to zero. From this condition, we obtain the value of ξ_3 :

$$\xi_3 = \sqrt{R(2\xi_0 + R)}, \quad (16)$$

and using Eq. (15) we then obtain

$$\sin \theta_3 = \frac{\sqrt{R(2\xi_0 + R)}}{R + \xi_0}. \quad (17)$$

Now, the x -momentum entering the control sphere from the upstream region can be calculated as :

$$\dot{I}_{x,in}(R) = 2\pi\rho_0 v_0 \int_0^{\xi_3} v_x(\xi, \theta_+) \xi d\xi, \quad (18)$$

where ξ_3 is given by Eq. (16), $v_x(\xi, \theta)$ by Eq. (6) and θ_+ is obtained with the + sign of Eq. (15). This integral can be solved analytically to obtain :

$$\dot{I}_{x,in}(R) = 4\pi\xi_0^2 \rho_0 v_0^2 f_{in}, \quad (19)$$

where

$$f_{in} = \frac{1 + 3w_0}{4w_0^2} -$$

$$\frac{1}{2} \left[\sqrt{1 + 2w_0} - 1 + (1 + w_0) \ln \left(\frac{1 + w_0}{1 + w_0 + \sqrt{1 + 2w_0}} \right) \right], \quad (20)$$

with $w_0 \equiv \xi_0/R < 1/2$.

The x -momentum rate leaving the control domain has two terms:

- the rate $\dot{I}_{x,b}$ of x -momentum leaving through the boundary of the spherical domain,
- the rate $\dot{I}_{x,a}$ of x -momentum hitting the symmetry axis and exiting the domain through a narrow wake along the x -axis.

The momentum rate leaving the sphere through the boundary of the control volume is given by :

$$\dot{I}_{x,b} = 2\pi\rho_0 v_0 \int_{\xi_2}^{\xi_3} v_x(\xi, \theta_-) \xi d\xi. \quad (21)$$

This integral can be performed analytically to obtain :

$$\dot{I}_{x,b} = 4\pi\xi_0^2 \rho_0 v_0^2 f_b, \quad (22)$$

where

$$f_b = \frac{1 + w_0}{4w_0^2} + \frac{1}{2} \left[1 + (1 + w_0) \ln \left(\frac{w_0}{1 + w_0} \right) \right]. \quad (23)$$

The momentum rate exiting the control region through the wake is given by :

$$\dot{I}_{x,a} = \int_{\xi_1}^{\xi_2} v_R d\dot{m}, \quad (24)$$

where

$$d\dot{m} = 2\pi\xi\rho_0 v_0 d\xi, \quad (25)$$

and the velocity v_R along the axis with which the material leaves the control domain is given by the kinetic+potential energy conservation condition

$$\frac{v_0^2}{2} - \frac{GM}{x_0} = \frac{v_R^2}{2} - \frac{GM}{R} \quad (26)$$

where x_0 is the distance along the x -axis at which the streamline intercepts the axis as given by Eq. (5). Here we have used that the x -component of the velocity is v_0 , as derived in Eq. (6). Using Eqs. (25-26), the integral in Eq. (24) can be performed analytically to obtain :

$$\dot{I}_{x,a} = 4\pi\xi_0^2 \rho_0 v_0^2 f_a, \quad (27)$$

where

$$f_a = \frac{1 - (2w_0)^{3/2}}{2w_0} + \frac{1}{\sqrt{1 + 2w_0}} \ln \left[\frac{2w_0 + \sqrt{2w_0(1 + 2w_0)}}{1 + \sqrt{1 + 2w_0}} \right]. \quad (28)$$

Finally, the net drag force of the gas on the body is obtained as :

$$F_d = \dot{I}_{x,in} - \dot{I}_{x,b} - \dot{I}_{x,a} = \frac{4\pi(GM)^2 \rho_0}{v_0^2} f(\xi_0, R), \quad (29)$$

where ξ_0 is given by Eq. (4) and

$$f(\xi_0, R) = f_{in} - f_b - f_a, \quad (30)$$

with f_{in} , f_b and f_a given by Eqs. (20), (23) and (28), respectively. Note that Equation (29) includes the force on the body due to momentum accretion (sometimes called as aerodynamic force).

It is straightforward to show that in the $R \gg \xi_0$ limit ($w_0 \ll 1$, see Eqs. 20, 23 and 28), this function takes the form

$$f(\xi_0, R) \approx \ln \left(\frac{2R}{\xi_0} \right) - \frac{1}{2} \left(1 - \frac{\xi_0}{R} \right). \quad (31)$$

A comparison between the full (Eq. 30) and approximate (Eq. 31) forms of f is shown in Fig. 3. It is clear that for radii larger than $\sim 5\xi_0$ the two forms of f agree to better than $\sim 10\%$.

From Eq. (31) we see that the drag force diverges logarithmically for large values of R , as occurs in linear perturbation theory. Therefore, it is possible to match the solution found in linear theory (Eq. 1), which is valid at far enough distances from the body, with that found in the nonlinear analysis. This can be accomplished by replacing R for $v_0 t$, where $t = 0$ is the time at which the body is formed¹. Moreover, we see that the ambiguity in the definition of the minimum radius r_{\min} that appears in linear theory is removed in our framework. In fact, we find that $r_{\min} = \sqrt{e}\xi_0/2$, where the factor \sqrt{e} comes from inserting the term $-1/2$ that appears in the right-hand-side of Equation (31) in the argument of the log.

¹ In a realistic situation, R will increase with time until it reaches the boundary of the cloud.

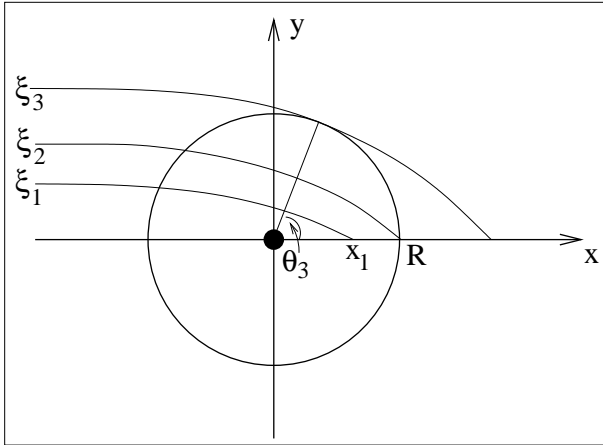


Figure 2. Schematic diagram showing the control sphere (of radius $R > x_1 = 2\xi_0$) and the three streamlines used in the calculation of the drag force (see section 3.2).

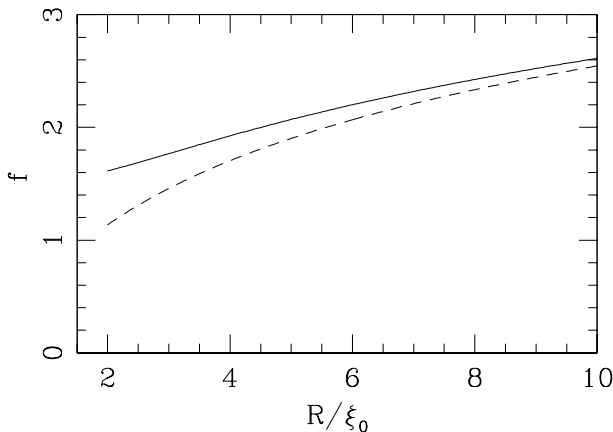


Figure 3. Exact (solid line, see Eq. 30) and approximate (dashed line, see Eq. 31) forms of the f function, which gives the dependence of the drag force as a function of the radius R of the control volume.

4 AN AXISYMMETRIC NUMERICAL SIMULATION

We have computed an axisymmetric numerical simulation, solving the Euler equations for an isothermal flow in a uniform, cylindrical computational grid. We have used the “flux vector splitting” algorithm of van Leer (1982), with the second order (time and space) implementation described by Raga et al. (2000).

The simulation that we are presented can be compared with the work of Ruffert (1996) and Moeckel & Throop (2009), who computed 3D simulations of basically the same physical situation. The main difference with this previous work is that our simulation is 2D (axisymmetric), and has ~ 2 orders of magnitude higher resolution.

The computational domain has an axial extent of $15\xi_0$ (with ξ_0 being the gravitational radius given by Eq. 4) and a radial extent of $7.5\xi_0$, resolved with 9000×4500 (axial \times radial) grid points. A point mass (influencing the flow only through its gravitational attraction) is placed in the middle of the axial extent of the domain. A spherical volume of

radius $0.05\xi_0$ (30 pixels) around the body is artificially kept at a low density at all times, so that the material entering this volume from the rest of the computational domain is effectively removed. We simulate in this way the accretion of gas onto the object.

In the left boundary of the domain we impose an inflow of density ρ_0 and velocity v_0 , parallel to the symmetry axis. A reflection condition is applied on the symmetry axis, and a zero gradient condition is applied in the remaining two boundaries of the computational domain. In the initial condition, the domain is filled with a uniform flow (of velocity v_0 and density ρ_0) parallel to the symmetry axis. The isothermal sound speed is chosen to be $c_0 = v_0/5$ (i.e., the flow entering the domain has a Mach number of 5).

The results obtained after time-integrations of 10, 40 and $70\xi_0/v_0$ are shown in Fig. 4. This figure is a zoom of an inner region of the computational domain, showing the highly time-dependent wake formed downstream of the body.

We take the density and flow velocity time-frames obtained from the simulation, and compute the net mass \dot{M}_{acc} , and momentum fluxes through a control sphere of arbitrary radius R centred on the point mass. Thereby, only \dot{M}_{acc} computed with $R = 2\xi_0$ corresponds exactly to the mass accretion rate onto the body. We also compute the gravitational force exerted on the body by the material within the control volume. In Fig. 5, we show the mass flux \dot{M}_{acc} , the drag force F_d and the gravitational force F_g computed with a control volume of radius $R = 5\xi_0$. F_g is inferred as the gravitational attraction between the body and the perturbed medium. \dot{M}_{acc} and F_d show a peak at $t \approx 5\xi_0/v_0$, and have fluctuating values for $t \geq 10\xi_0/v_0$. The gravitational force F_g initially grows as more material enters the wake behind the object, and also shows fluctuating values as a function of time. The fact that \dot{M}_{acc} , F_d and F_g have strong fluctuations is not surprising given the strongly time-dependent structure of the flow (see Fig. 4).

In order to carry out a comparison with the analytic model (see section 3.2), we have calculated the average values and the dispersions of \dot{M}_{acc} , F_d and F_g in the interval $10\xi_0/v_0 \leq t \leq 66\xi_0/v_0$, in which the fluctuations of these quantities appear to be statistically stationary (see Fig. 5). We then plot these time-averaged values as a function of the radius R of the control volume in Fig. 6.

We have considered control volumes with radii $2\xi_0 \leq R \leq 7\xi_0$, the lower boundary being fixed by the derivation of the analytic model (in which it was assumed that $R \geq 2\xi_0$, see section 3) and the upper boundary given by the approach to the outer edge of the computational grid. It is clear from Fig. 6 that the dispersions of the \dot{M}_{acc} and F_d values grow as a function of R (due to the fact that larger, more massive eddies are seen at larger distances downstream from the body, see Fig. 4), while the dispersion of F_g (which is a quantity integrated over the volume of the control sphere) remains approximately constant.

The analytic model predicts that $\dot{M}_{acc} = 4\pi\xi_0^2\rho_0v_0$ (see Eq. 14) for all control spheres with $R \geq 2\xi_0$. The top panel of Fig. 6 shows that the time-averaged values obtained from the numerical simulation closely reproduce this result. The central panel of Fig. 6 shows the drag force F_d calculated using Eq. (29), which has values that differ from the results from the numerical simulations by less than $\sim 15\%$ (though

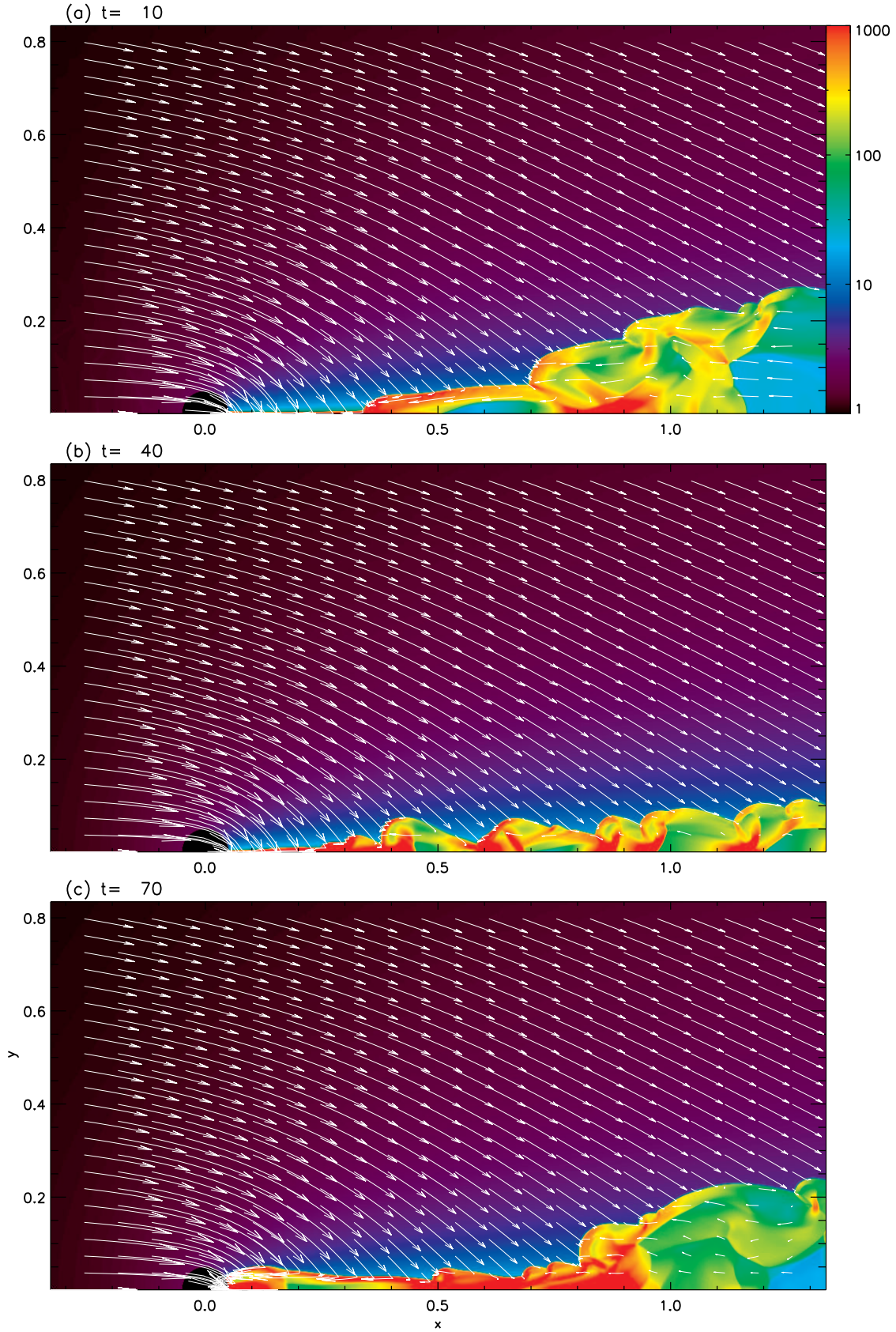


Figure 4. Density (in units of ρ_0 , with the colour scale given by the top right bar) and velocity field (white arrows) from the axisymmetric simulation described in section 4, obtained for integration times $t = 10\xi_0/v_0$ (panel a), $40\xi_0/v_0$ (panel b) and $70\xi_0/v_0$ (panel c). The axes are in units of ξ_0 . The perturber is on the abscissa at position $x = 0$, and the flow enters the domain from the left. Only a limited region of the computational domain is shown (see section 4). The x (symmetry axis) and y (cylindrical radius) axes are labeled in units of ξ_0 .

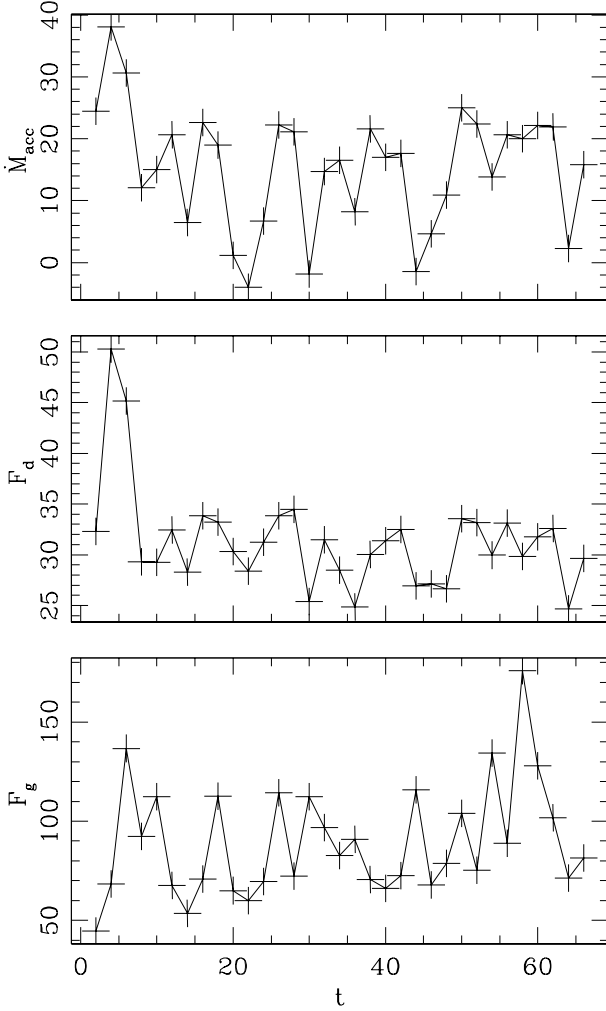


Figure 5. Mass flux (in units of $\xi_0^2 \rho_0 v_0$, top), drag force (in units of $\xi_0^2 \rho_0 v_0^2$, centre) and gravitational force on the body (in units of $\xi_0^2 \rho_0 v_0^2$, bottom) as a function of time (in units of ξ_0/v_0). These parameters were computed from the results of the axisymmetric simulation (described in the text) using a spherical control volume of radius $R = 5\xi_0$.

the slope of the F_d vs. R dependence appears to be higher in the numerical results than in the analytic model).

In the bottom panel of Fig. 6 we show the gravitational force on the body due to the density structure of the numerical model. The gravitational force is larger than the net drag because momentum accretion onto the body produces an accelerating force. We also plot the gravitational force from the numerical simulation but excluding the contribution from the dense wake behind the shock (see the lower sequence of points in the bottom frame of Fig. 6). This force is comparable to the one obtained from the analytic density stratification given by Eq. (7), which only refers to the material in the free-streaming region before entry into the axial wake. A comparison between the gravitational force with (upper sequence of points) and without (lower sequence) the material within the wake indicates that $\sim 90\%$ of the gravitational force on the body comes from the material within the wake.

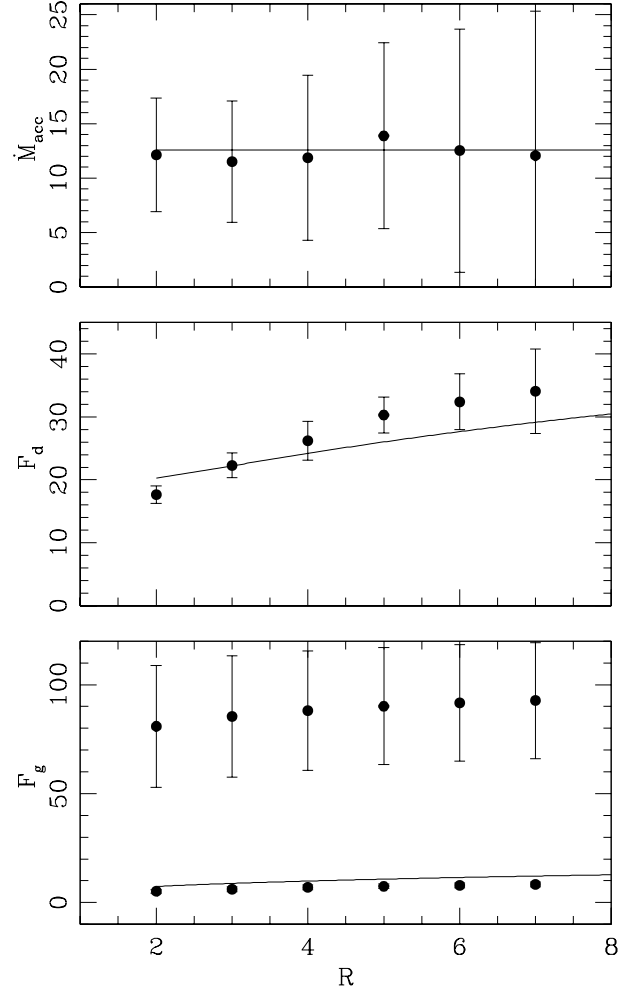


Figure 6. Time-averaged values of the net mass flux (in units of $\xi_0^2 \rho_0 v_0$, top), drag force (in units of $\xi_0^2 \rho_0 v_0^2 = (GM)^2 \rho_0 / v_0^2$, centre) and gravitational force on the body (in the same units, bottom) as a function of the radius R of the control volume (R is given in units of ξ_0). The dispersions are indicated by the error bars. The gravitational force has been calculated in two ways: considering the contribution of all of the gas within the control sphere (sequence of points on the upper part of the bottom frame), and eliminating the contribution of the material within the wake (lower sequence of points, bottom frame). The solid lines are the predictions from the analytic model described in section 3.

5 SUMMARY

We present an analytic model for the flow generated by a point mass moving hypersonically within a homogeneous environment. This model is based on the ballistic orbit theory (see, e. g., Bisnovaty-Kogan et al. 1979), and is developed so as to obtain analytic expressions for the mass accretion rate and the non-linear gravitational drag. Since we include the contribution of the non-linear inner wake, there is no ambiguity in the definition of the minimum cut-off distance of the interaction, which turns out to be $\simeq 0.82\xi_0$.

We find that the predicted mass accretion rate and gravitational drag agree satisfactorily with the results from an axisymmetric, isothermal simulation:

- For the mass accretion rate we essentially find full agree-

ment between the analytic and numerical results (see Eq. 14 and Fig. 6). This result in principle differs from the one of Moekel & Throop (2009), who obtain a significantly lower value for the accretion rate from their numerical simulation. The fact that we obtain a better agreement could be due to the considerably higher resolution of our simulation, or to the fact that we carry out a much longer time-integration (extending to $\sim 70\xi_0/v_0$, compared to $\sim 1.5\xi_0/v_0$ for the simulation of Moekel & Throop 2009).

- For the net drag force F_d we obtain an agreement within $\sim 20\%$ between the prediction from the analytic model and the numerical simulations (see Fig. 6). Though the analytic and numerical drag forces have a reasonable quantitative agreement, it appears that the analytic model predicts a shallower F_d vs. R dependence (where R is the radius of the control volume enclosing the material assumed to produce the drag) than the one obtained from the numerical simulation (see Fig. 6).

There are several possible sources for this discrepancy between the analytic and numerical drag forces. It appears that the limited numerical resolution of the simulation is not responsible for this effect, because we have repeated the simulation at 1/2 and 1/4 of the resolution (of the simulation presented in section 4) and obtain basically the same drag force. A possible source of the differences between the analytic and numerical F_d is the fact that the simulation has a finite Mach number ($\mathcal{M} = 5$ for the upstream flow, see section 4), while the analytic model essentially has an infinite Mach number (i.e., zero gas pressure). Another difference is that the numerical simulation has a rather broad wake region, while in the analytic solution it is assumed that the tail occupies a very narrow region surrounding the symmetry axis. A third difference is that while in the analytic model the perturbed environmental gas effectively extends to infinity, the numerical simulation of course is carried out in a finite domain (see section 4). Given these clear differences between the numerical and analytic models, the agreement that we find between the two can be regarded as quite successful.

In this paper we have therefore derived an analytic recipe for the drag force F_d (from a ballistic flow model), which is successfully reproduced by an axisymmetric numerical simulation. This recipe for F_d will be useful for carrying out simulations of compact bodies in motions influenced by gravitational drag. Possible examples are the motions of young stars within molecular clouds (see, e. g., Throop & Bally 2008; Chavarría et al. 2010), or the orbital decay of black holes in the centre of merging galaxies (Narayan 2000; Escala et al. 2004, 2005; Dotti et al. 2006). Kim & Kim (2009) computed the nonlinear gravitational drag on a massive Plummer perturber in adiabatic axisymmetric simulations and found that it is smaller than the linear theory predicts for supersonic bodies. This reduction of the drag force is accounted for correctly in our drag formula.

ACKNOWLEDGMENTS

We acknowledge support from the CONACyT grants 60526, 61547, 101356 and 101975.

REFERENCES

- Chandrasekhar, S. 1943, *ApJ*, 97, 255
 Bisnovatyi-Kogan, G. S., Kazhdan, Ya. M., Klypin, A. A., Lutskii, A. E., Shakura, N. I. 1979, *Soviet Astron.*, 23, 201
 Bondi, H., Hoyle, F. 1944, *MNRAS*, 104, 273
 Chavarría, L., Mardones, D., Garay, G., Escala, A., Bronfman, L., Lizano, S. 2010, *ApJ*, 710, 583
 Conroy, C., Ostriker, J. P. 2008, *ApJ*, 681, 151
 Dokuchaev, V. P. 1964, *Soviet Astron.*, 8, 23
 Dotti, M., Colpi, M., Haardt, F. 2006, *MNRAS*, 367, 103
 Edgar, R. 2004, *New Astr. Rev.*, 48, 843
 Escala, A., Larson, R. B., Coppi, P. S., Mardones, D. 2004, *ApJ*, 607, 765
 Escala, A., Larson, R. B., Coppi, P. S., Mardones, D. 2005, *ApJ*, 630, 152
 Fryxell, B. A., Taam, R. E., McMillan, S. L. W. 1987, *ApJ*, 315, 536
 Hoyle, F., Lyttleton, R. A. 1939, *Proc. Cam. Phil. Soc.*, 35, 405
 Just, A., Kegel, W. H. 1990, *A&A*, 232, 447
 Kim, W.-T. 2007, *ApJ*, 667, L5
 Kim, W.-T. 2010, *ApJ*, 725, 1069
 Kim, H., Kim, W.-T. 2007, *ApJ*, 665, 432
 Kim, H., Kim, W.-T. 2009, *ApJ*, 703, 1278
 Koide, H., Matsuda, T., Shima, E. 1991, *MNRAS*, 252, 473
 Lyttleton, R. A. 1972, *MNRAS*, 160, 255
 Moekel, N., Throop, H. B. 2009, *ApJ*, 707, 258
 Naiman, J. P., Ramírez-Ruiz, E., Lin, D. N. C. 2011, *arXiv:1104.3140*
 Namouni, F. 2010, *MNRAS*, 401, 319
 Narayan, R. 2000, *ApJ*, 536, 663
 Nejad-Asghar, M. 2010, *MNRAS*, 406, 1253
 Ostriker, E. C. 1999, *ApJ*, 513, 252
 Raga, A. C., Navarro-González, R., Villagrán-Muniz, M. 2000, *RMxAA*, 36, 67
 Rephaeli, Y., Salpeter, E. E. 1980, *ApJ*, 240, 20
 Ruderman, M. A., Spiegel, E. A. 1971, *ApJ*, 165, 1
 Ruffert, M. 1996, *A&A*, 311, 817
 Sánchez-Salcedo, F. J. 2009, *MNRAS*, 392, 1573
 Sánchez-Salcedo, F. J., Brandenburg, A. 1999, *ApJ*, 522, L35
 Sánchez-Salcedo, F. J., Brandenburg, A. 2001, *MNRAS*, 322, 67
 Shima, E., Matsuda, Y., Takeda, H., Sawada, K. 1985, *MNRAS*, 217, 367
 Tanaka, T., Haiman, Z. 2009, *ApJ*, 696, 1798
 Throop, H. B., Bally, J. 2008, *AJ*, 135, 2380
 van Leer, B. 1982, *ICASE Report No. 82-30*
 Villaver, E., Livio, M. 2009, *ApJ*, 705, L81

This paper has been typeset from a \LaTeX file prepared by the author.